

# Quantum-enhanced magnetometry by phase estimation algorithms with a single artificial atom

S. Danilin,<sup>1</sup> A. V. Lebedev,<sup>2,3</sup> A. Vepsäläinen,<sup>1</sup> G. B. Lesovik,<sup>2</sup> G. Blatter,<sup>3</sup> and G. S. Paraoanu<sup>1</sup>

<sup>1</sup>*Low Temperature Laboratory, Department of Applied Physics,*

*Aalto University School of Science, PO Box 15100, Aalto FI-00076, Finland*

<sup>2</sup>*Moscow Institute of Physics and Technology, Institutskii per. 9, Dolgoprudny, 141700, Moscow District, Russia*

<sup>3</sup>*Theoretische Physik, Wolfgang-Pauli-Strasse 27, ETH Zürich, CH-8093 Zürich, Switzerland*

(Dated:)

Phase estimation algorithms are key protocols in quantum information processing. Besides applications in quantum computing, they can also be employed in metrology as they allow for fast extraction of information stored in the quantum state of a system. Here, we implement two suitably modified phase estimation procedures, the Kitaev- and the semiclassical Fourier-transform algorithms, using an artificial atom realized with a superconducting transmon circuit. We demonstrate that both algorithms yield a flux sensitivity exceeding the classical shot-noise limit of the device, allowing one to approach the Heisenberg limit. Our experiment paves the way for the use of superconducting qubits as metrological devices which are potentially able to outperform the best existing flux sensors with a sensitivity enhanced by few orders of magnitude.

PACS numbers: 85.25.Cp, 06.20.-f, 03.67.-a

Phase estimation algorithms are the building elements for many important quantum algorithms<sup>1</sup>, such as Shor's factorization algorithm<sup>2,3</sup> or Lloyd's algorithm<sup>4</sup> for solving systems of linear equations. At the same time, phase estimation is a natural concept in quantum metrology<sup>5</sup>, where one aims at evaluating an unknown parameter  $\lambda$  that typically enters into the Hamiltonian of a probe quantum system and defines its energy states  $E_n(\lambda)$ . In a standard (classical) measurement, the precision  $\delta\lambda$  is restricted by the shot-noise limit  $\delta\lambda \propto 1/\sqrt{t}$ , where  $t$  is the measurement time. This, however, is not a fundamental limit: in principle, the ultimate attainable precision scales as  $\delta\lambda \propto 1/t$ , constrained only by the Heisenberg relation  $\Delta E(\lambda) \geq 2\pi\hbar/t$ , where  $\Delta E = \max_{n,m}(E_n - E_m)$ . The Heisenberg limit can be achieved with the help of entanglement resources, e.g., using NOON photon states in optics<sup>7-9</sup>. However, these states are difficult to create in general and they typically have a short coherence time. Alternatively, one can achieve the Heisenberg limit without exploiting entanglement, by using the coherence of the wavefunction of a quantum system as a dynamical resource. However, the uncontrollable interaction of the probe with the environment limits the time scale  $t$  where the Heisenberg scaling can be attained by the probe's coherence time  $t \sim T_2$ . A further improvement then makes use of an alternative measurement strategy with a precision following the standard quantum limit but with a better prefactor.

The unknown parameter  $\lambda$  can be estimated from the phase  $\phi = \Delta E(\lambda)\tau/\hbar$  accumulated by the system in the course of its evolution during the time  $\tau \sim T_2$ . The  $2\pi$ -periodicity of the phase limits the probes' measurement range  $\Delta\lambda$  where  $\lambda$  can be unambiguously resolved to the narrow interval  $[\delta\lambda]_{\text{H}} = 2\pi\hbar/(\mu T_2)$ , with  $\mu \equiv \partial\Delta E/\partial\lambda$  denoting the sensitivity of the probe's spectrum. Therefore, the improvement in the precision for larger  $T_2$  is concomitant with a proportional reduction of the mea-

surement range  $\Delta\lambda$ . The use of phase estimation algorithms then allows to resolve the  $2\pi$  phase uncertainty and hence break this unfavorable trade-off between the measurement precision  $\delta\lambda$  and the measurement range  $\Delta\lambda$ . Moreover, a metrological procedure based on a phase estimation algorithm is Heisenberg-limited: it attains the resolution  $\delta\lambda \sim [\delta\lambda]_{\text{H}}$  within a large measurement range  $\Delta\lambda \gg [\delta\lambda]_{\text{H}}$  with a Heisenberg scaling in the phase accumulation time  $\tau$ , i.e.,  $\delta\lambda \propto \hbar/(\mu\tau)$  for  $\tau \leq T_2$ . At larger times  $\tau > T_2$ , the measurement proceeds with independent measurements involving the optimal time delay  $\tau = T_2$ . Running  $N = t/T_2$  experiments and averaging over  $N \gg 1$  outcomes, one can further improve the precision within the standard quantum limit<sup>6</sup>,  $\delta\lambda \propto 2\pi\hbar/(\mu T_2\sqrt{N}) \equiv 2\pi\hbar/(\mu\sqrt{tT_2})$ .

There are two major classes of phase estimation algorithms, one suggested early on by Kitaev<sup>10</sup> and a second originating from the quantum Fourier transform<sup>11,12</sup>. In quantum computing, the Kitaev algorithm was run as part of Shor's factorization algorithm<sup>16</sup> and the Fourier transform algorithm was used in optics to measure frequencies<sup>17</sup>. These algorithms are system-independent and can be implemented in a variety of experimental settings, e.g., using NV centers in diamond for the sensitive detection of magnetic fields<sup>13-15</sup>.

Here, we implement a modified version of these algorithms using an artificial atom or qubit in the form of a superconducting transmon circuit<sup>18</sup>. We show that the transmon can be operated as a dc flux magnetometer with Heisenberg-limited sensitivity. The sensitivity is boosted by a magnetic moment that is about five orders of magnitude larger than that of natural atoms or ions. The idea of the experiment is to combine the extreme magnetic-field sensitivity of superconducting quantum interference devices (SQUIDs) with an enhanced performance brought about by exploiting quantum coherence. The 'quantum' in the name of this device refers to the

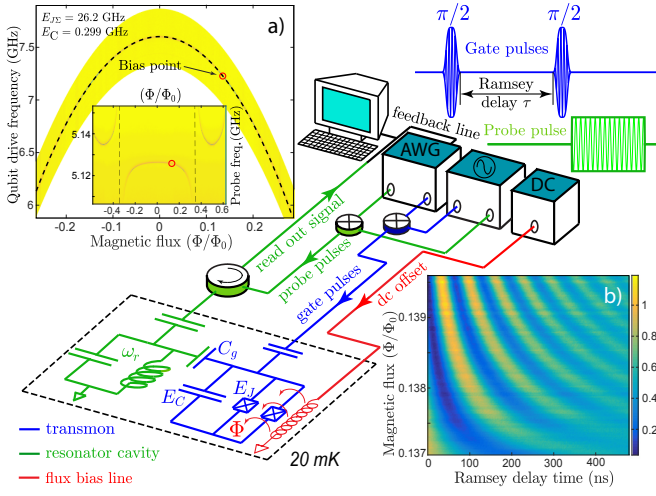


**FIG. 1: Experimental layout.** The schematic shows a transmon qubit (in blue) comprised of a capacitor and a SQUID loop with two nearly identical junctions. The qubit charging and total Josephson energies are  $E_C = 299$  MHz and  $E_{J\Sigma} = 26.2$  GHz. The qubit is coupled via a gate capacitor  $C_g$  to a coplanar waveguide resonator (CPW, in green) with a resonance frequency  $\omega_r$  around  $2\pi \times 5.12$  GHz. The magnetic flux  $\Phi$  through the transmon's SQUID loop is controlled by a dc-current flowing through a flux-bias line (in red). An arbitrary waveform generator (AWG) and a microwave analog signal generator are employed to create a Ramsey sequence of two  $\pi/2$  microwave pulses at a carrier frequency  $\omega_d = 2\pi \times 7.246$  GHz separated by a time delay  $\tau$ . The sequence drives the transmon into a superposition of ground and excited states where the state amplitudes depend on the accumulated phase  $\phi = [\omega_d - \omega_{01}(\Phi)]\tau$ . The qubit state is read out nondestructively using a probe pulse sent to the CPW resonator; the reflected signal is downconverted (not shown in the figure), digitized, and analyzed by a computer. Next, the computer updates a flux distribution function  $\mathcal{P}(\Phi)$  stored in its memory, determines the next optimal Ramsey delay time, and feeds it back into the AWG. **a)** Qubit transition frequency  $\omega_{01}(\Phi)$  as a function of magnetic flux  $\Phi$  (parabolic curve). The bottom inset shows the CPW resonator's spectrum. The red circles indicate the bias point of our transmon sensor: we operate far away from the 'sweet spot' in a regime where the transmon's frequency  $\omega_{01}(\Phi)$  is an approximately linear function of the flux  $\Phi$  within the entire flux range  $\Delta\Phi$ . For the fluxes around the point considered here, the frequency  $\omega_r$  of the readout CPW resonator remains approximately constant. **b)** A pre-measured sample-specific Ramsey interference fringes pattern defines the 'passport' function of our sensor. This can be regarded as a non-normalized probability function  $P_p(\tau, \Phi)$  to observe the qubit in the excited state after a Ramsey sequence with a delay  $\tau$  for a specific value of the magnetic flux  $\Phi$ . The largest flux value used to obtain the Ramsey interference fringes pattern  $\Phi = 0.1394\Phi_0$  corresponds to a frequency detuning  $\Delta\omega = \omega_d - \omega_{01}(\Phi) = 2\pi \times 15.8$  MHz between the drive and the qubit transition frequencies. The flux range of the 'passport'  $\Delta\Phi \sim 2.5 \times 10^{-3}\Phi_0$  corresponds to a range  $2\pi \times 13.8$  MHz in frequency detuning.

macroscopic complex wave function of the superconducting electronic state. In the SQUID loop geometry, the relative phase of the superconducting wavefunctions across the Josephson junctions acquires a dependence on magnetic flux  $\Phi$  via the Aharonov-Bohm effect. However, despite its quantum origin, in standard SQUID measurements this phase is a classical variable. In contrast, for the SQUID loop of a transmon qubit, the phase turns into a fully dynamical quantum observable and the flux  $\Phi$  dependence is encoded in the energy-level separation  $\hbar\omega_{01}(\Phi)$  between the ground state and the first excited state. Therefore, it is possible to exploit the phase difference  $\phi = [\omega_d - \omega_{01}(\Phi)]\tau$  acquired during a time  $\tau$  by the qubit when it is prepared into a coherent superposition of the ground and excited energy states and driven by an external microwave field at a frequency  $\omega_d$ . Differently from their "natural" counterparts, where the characteristics of the quantum sensor are sample independent and defined by the atomic structure, for artificial-atom systems, such as the transmon, we need to adapt the algorithms by including device-specific properties in a so-called *passport* – a sample specific Ramsey interference pattern obtained in advance from characterization measurements, see Fig. 1b). Making use of phase estimation algorithms, we demonstrate an enhanced dc-flux sensitivity of the transmon sensor in an enlarged flux range as compared to standard (classical) measurement schemes. Recently, a standard measurement procedure using a flux qubit has been used for the measurement of an ac-magnetic field signal<sup>19</sup>.

The experiment employs a superconducting circuit in a transmon configuration, consisting of a capacitively-shunted split Cooper-pair box coupled to a  $\lambda/4$ -wavelength coplanar waveguide (CPW) resonator realized in a 90 nm thick aluminum film deposited on the surface of a silicon substrate, see Fig. 1 and SI 1 for an image of the sensor device. The SQUID loop of the transmon has an area of  $S \simeq 600 \mu\text{m}^2$ , which is chosen large in comparison with standard transmon qubit designs in order to provide a higher sensitivity to magnetic-field changes. The magnetic moment of this artificial atom is  $\mu = S\hbar|d\omega_{01}/d\Phi|$ , directly proportional to the area  $S$  and the rate of change with flux  $\Phi$  of the transition frequency  $\omega_{01}$ . For our device, we obtain  $d\omega_{01}/d\Phi = -2\pi \times 5.3$  GHz/ $\Phi_0$  at the bias point, resulting in  $\mu = 1.10 \times 10^5 \mu_B$ , where  $\mu_B$  is the Bohr magneton. By comparison, the Zeeman splitting due to the magnetic moment of NV centers is  $28$  GHz  $\text{T}^{-1}$ , corresponding to a magnetic moment of  $2\mu_B$ . The sample is thermally anchored to the mixing chamber plate of a dilution refrigerator and cooled down to a temperature of roughly  $\sim 20$  mK. The qubit has a separate flux-bias line and a microwave gate line, the former allowing to change the qubit transition frequency, while the latter is used for the qubit's state manipulation. The qubit state is determined by a nondemolition read-out technique (see Methods and SI 1) measuring the probe signal reflected back from the dispersively-coupled CPW resonator. To

increase the magnetic field sensitivity, we bias the qubit away from the 'sweet spot', see Fig. 1a). This follows an opposite strategy as compared to the situation where the phase estimation algorithms are employed for quantum computing and simulations; in the latter cases, the qubit sensitivity to flux noise is maximally suppressed by tuning the device to the 'sweet spot' characterized by a vanishing first derivative of the energy with respect to flux. Operating away from the 'sweet spot' leads to a reduction of the  $T_2$  time. The decoherence rate  $T_2^{-1} = (2T_1)^{-1} + T_\phi^{-1}$  is the sum of the relaxation  $(2T_1)^{-1}$  and dephasing  $T_\phi^{-1}$  rates<sup>22</sup>. The dephasing rate appreciably increases at our bias point, which reduces  $T_2$  and thus the number of available steps that can be implemented in the Kitaev- and Fourier algorithms.

In the experiment, we apply a Ramsey sequence of two consecutive  $\pi/2$  pulses separated by a time delay  $\tau$ , which corresponds to an effective spin-1/2 precession around the z-axis of the Bloch sphere. The precession angle  $\phi = \Delta\omega(\Phi)\tau$  is defined by the frequency mismatch  $\Delta\omega(\Phi) = \omega_d - \omega_{01}(\Phi)$  between the transition frequency  $\omega_{01}(\Phi)$  of the transmon qubit and the fixed drive frequency  $\omega_d$  of the  $\pi/2$  pulses. The Ramsey sequence drives the transmon from its ground state into a coherent superposition of ground- and excited states with relative amplitudes determined by the phase  $\phi$ . The theoretical probability to find the transmon in the first excited state is given by

$$P[\tau, \Delta\omega(\Phi)] = \frac{1}{2} + \frac{1}{2} \exp(-\tau/2T_1) \gamma(\tau) \cos[\Delta\omega(\Phi)\tau] \quad (1)$$

and depends both on the delay time  $\tau$  and on the magnetic flux  $\Phi$  through the frequency mismatch  $\Delta\omega(\Phi)$ . The decay function  $\gamma(\tau)$  accounts for the dephasing of the transmon. The dephasing process can be described through an external classical noise source, see Methods. The particular shape of  $\gamma(\tau)$  depends on the noise spectral density at low frequencies. 'White' noise with a constant power density results in an exponential decay function  $\gamma(\tau) = \exp(-\Gamma_{\text{exp}}\tau)$ , while  $1/f$ -noise produces a Gaussian decay  $\gamma(\tau) = \exp[-(\Gamma_{1/f}\tau)^2]$ . A transmon atom is insensitive to background charge fluctuations and the external noise originates from magnetic flux fluctuations, with  $1/f$ -noise turning out to be a more relevant source of dephasing for flux qubits<sup>20</sup>. We fit our experimental curves  $P(\tau, \Delta\omega(\Phi))$  by Eq. (1) using both an exponential and a Gaussian decay, see SI 2. For our sample with a relaxation time  $T_1$  of about 260 ns, we cannot distinguish between these two fits, neither in the 'sweet spot' nor in the bias point. Fitting the Ramsey oscillation at different fluxes one finds  $\Gamma_{\text{exp}}^{-1} \approx 1250$  ns and  $\Gamma_{1/f}^{-1} \approx 780$  ns at the 'sweet spot'. At the bias point, these pure dephasing times reduce to 520 ns and 420 ns, respectively. The decay rates  $\Gamma_{\text{exp}}$  and  $\Gamma_{1/f}$  in the bias point can be translated into corresponding strengths of magnetic flux fluctuations of  $6.2 \times 10^{-8} \Phi_0 \text{Hz}^{-1/2}$  and  $9 \times 10^{-5} \Phi_0$  for the white and  $1/f$  noise, respectively.

The function  $\gamma(\tau)$  determines the optimal delay time  $\tau$  where the sensitivity of the probability  $P(\tau, \Delta\omega)$  to the changes in  $\Delta\omega$  and hence to a flux is the highest. In the standard (classical) measurement approach, a minimal delay  $\tau = \tau_0 \ll T_2$  sets the frequency range  $\Delta\omega(\Phi) \in [0, \pi/\tau_0]$  where the phase  $\phi$  and hence  $P(\tau, \Delta\omega)$  can be unambiguously resolved. This defines the range  $\Delta\Phi = \pi(\tau_0 d\omega_{01}/d\Phi)^{-1}$  where the magnetic flux can be resolved with a precision scaling given by the standard quantum limit (see Methods),

$$[\delta\Phi]_{\text{class}} = \left| \frac{d\omega_{01}(\Phi)}{d\Phi} \right|^{-1} \frac{1}{\tau_0 \sqrt{t/T_{\text{rep}}}} = \frac{A_{\text{class}}}{\sqrt{t}}, \quad (2)$$

where  $t$  is the total measurement or *sensing* time of the experiment and  $T_{\text{rep}}$  is the time duration of a single Ramsey measurement. A better flux sensitivity can be attained at larger delays  $\tau$ , where the probability  $P[\tau, \Delta\omega(\Phi)]$  is more sensitive to changes in  $\Delta\omega$ . We obtain the best sensitivity at  $\tau = \tau^*$  defined by the condition  $(2T_1)^{-1} - [\ln \gamma(\tau)]' = \tau^{-1}$  (see Methods),

$$[\delta\Phi]_{\text{quant}} = \left| \frac{d\omega_{01}(\Phi)}{d\Phi} \right|^{-1} \frac{e}{\tau^* \sqrt{t/T_{\text{rep}}}} = \frac{A_{\text{quant}}}{\sqrt{t}}. \quad (3)$$

Measuring at the optimal delay  $\tau = \tau^*$  improves the flux resolution by a factor  $A_{\text{class}}/A_{\text{quant}} = \tau^*/(e\tau_0)$ , which depends on the qubit's coherence time, the latter serving as the quantum resource in our algorithms. Another important factor which enhances the flux sensitivity is the slope  $d\omega_{01}/d\Phi$  of the transmon's spectrum. At our working point  $\omega_{01} = 2\pi \times 7.246$  GHz, we have  $d\omega_{01}/d\Phi = -2\pi \times 5.3$  GHz/ $\Phi_0$ . The minimal delay is given by  $\tau_0 \approx 31.6$  ns, see SI 1. The repetition time  $T_{\text{rep}} = 6.546$   $\mu\text{s}$  involves the maximal time duration of the Ramsey sequence, the duration of the probe pulse (2  $\mu\text{s}$ ) and the transmon's relaxation time back into its ground state (4  $\mu\text{s}$ , which is 15 times longer than the  $T_1$  time). Combining these numbers and setting  $\tau^* \sim 2T_1$ , we estimate the theoretical value of flux sensitivity for our transmon sensor as  $A_{\text{quant}} \simeq 4 \times 10^{-7} \Phi_0 \text{Hz}^{-1/2}$ , see Eq. (3), providing an improvement by a factor  $A_{\text{class}}/A_{\text{quant}} \sim 6$  over the classical sensitivity. Note, that the best sensitivity is attained at  $T_{\text{rep}} = \tau^*$  (i.e., for a very fast control and readout) that gives for our sample  $[\delta\Phi]_{\text{quant}} \simeq 1.1 \times 10^{-7} \Phi_0 \text{Hz}^{-1/2} / \sqrt{t}$ .

Measuring at large time delays  $\tau \sim T_2$  leaves an uncertainty in  $\Delta\omega(\Phi)$  due to the multiple  $2\pi$ -winding of the accumulated phase, thereby squeezing the flux range  $\Delta\Phi \sim 2.5 \times 10^{-3} \Phi_0$  by the small factor  $\tau_0/T_2$ . The Kitaev- and Fourier phase estimation algorithms, avoid this phase uncertainty by measuring the probability  $P(\tau, \Delta\omega)$  at different delays  $\tau_k = 2^k \tau_0$  for  $K \sim \log_2(T_2/\tau_0)$  consecutive steps  $k = 0, \dots, K-1$ . As a result, such a metrological procedure is able to resolve the magnetic flux with the quantum limited resolution  $[\delta\Phi]_{\text{quant}}$ , see Eq. (3), within the original flux range  $\Delta\Phi$  set by the duration  $\sim \tau_0$  of the control rf-pulses. The operation of the Kitaev and Fourier metrological procedures can be viewed

as a successive determination of the binary digits of the index  $n = [b_{K-1} \dots b_0] \equiv \sum_{k=0}^{K-1} b_k 2^k$  in the so-called quantum abacus<sup>23</sup>. The Kitaev algorithm starts from a minimal delay  $\tau = \tau_0$  and determines the most significant bit  $b_{K-1}$  in its first step, further proceeding with the less significant bits  $b_{K-2}, \dots, b_0$ . The Fourier algorithm works backwards<sup>24</sup>: it starts from the maximal delay  $\tau \sim T_2$  and first determines the least significant bit  $b_0$ , then gradually learns more and more significant bits  $b_1, b_2, \dots, b_{K-1}$ .

**Modified Kitaev- and Fourier metrological algorithms.** In the present work, we use modified versions of the phase estimation protocols, which take into account the nonidealities present in actual experiments. For brevity, we will still refer to these protocols as the Kitaev- and Fourier phase estimation algorithms. We demonstrate the superiority of these algorithms over the standard technique and show that we can beat the standard quantum limit. Instead of relying on the ideal theoretical probability function  $P[\tau, \Delta\omega(\Phi)]$  of Eq. (1) these modified Kitaev and Fourier protocols exploit the empirical probability  $P_p(\tau, \Phi)$ , the so-called passport, which we measure by a set of Ramsey sequences at various magnetic fluxes  $\Phi$ , representing the result on a discrete equidistant grid in the form  $P_p(\tau_j, \Phi_i)$ , see Fig. 1b). Here,  $\Phi_i = (i-1)[\delta\Phi]_{\text{step}} + \Phi_1$  with the index  $i$  chosen from the flux-index set  $I_0 = [1, 161]$ ,  $[\delta\Phi]_{\text{step}} \simeq 1.59 \times 10^{-5} \Phi_0$ ,  $\Phi_1 \simeq 0.137 \Phi_0$ , and discrete time delays  $\tau_j = (j-1) \times 2$  ns,  $j = 1, \dots, 241$  quantifying the time separation between the two  $\pi/2$  rf-pulses of the Ramsey sequence. In order to increase the signal-to-noise ratio, we average over 65000 Ramsey experiments at each discrete point  $(\tau_j, \Phi_i)$ . The resulting pattern is only approximately described by Eq. (1) due to the fact that the resonator frequency changes slightly with the applied flux, thus modifying our calibration (see Methods and SI 2). In principle, one can change the working point to an even more sensitive part of the spectrum at the price of a further distortion of this pattern.

Using the qubit passport  $P_p(\tau_j, \Phi_i)$ , one can pose the following metrological question: given an unknown flux  $\Phi$  within some pre-chosen range, how can one estimate its value using a minimal number of Ramsey measurements? We design two metrological algorithms where the time delay  $\tau$  of the Ramsey sequence serves as an adaptive parameter whose value is dynamically adjusted. In the course of operation, both our algorithms return a discrete probability distribution  $\mathcal{P}(\Phi_i)$ ,  $i \in I_0$ , which reflects our current knowledge about the flux  $\Phi$  to be measured. This probability distribution is improved in subsequent steps and shrinks to a narrow interval around the actual flux-value when running the algorithm.

**Bayesian learning.** The elementary building block for both our metrological algorithms is a Bayesian learning subroutine which updates the discrete flux distribution  $\mathcal{P}(\Phi_i)$  after each Ramsey measurement of the qubit state. This subroutine takes the time delay  $\tau_j$  between  $\pi/2$  pulses as an input parameter and performs a se-

quence of  $N = 32$  Ramsey measurements. Our readout scheme returns a measured variable  $h_N$  which, at  $N \gg 1$ , is equal to the empirical passport probability  $P_p(\tau_j, \Phi_i)$ . At small values  $N$ , the readout variable  $h_N$  is a normally distributed random variable with a mean value given by  $P_p(\tau_j, \Phi_i)$ ,

$$p(h_N|\tau_j, \Phi_i) = \frac{1}{\sqrt{2\pi}\sigma_N} \exp\left[-\frac{(h_N - P_p(\tau_j, \Phi_i))^2}{2\sigma_N^2}\right], \quad (4)$$

where the variance  $\sigma_N^2 = \sigma_1^2/N$  can be directly measured,  $\sigma_1^2 \approx 3.5$  (see SI 1 for further explanations on the readout variable  $h_N$ ). Next, the algorithm makes use of the measurement outcomes  $h_N$  and updates the flux probability distribution with the help of Bayes' rule,  $\mathcal{P}(\Phi_i) \rightarrow p(h_N|\tau_j, \Phi_i) \mathcal{P}(\Phi_i) / \sum_i p(h_N|\tau_j, \Phi_i) \mathcal{P}(\Phi_i)$ .

**Kitaev algorithm.** The Kitaev-type metrological algorithm has been introduced earlier in Ref. 25. The algorithm involves  $K$  steps  $k = 0, \dots, K-1$  with optimized Ramsey times  $\tau_k$ , tolerances  $\epsilon_k$ , and flux index sets  $I_k$ ; below,  $\mathcal{N}(I)$  denotes the size of a discrete set  $I$ . It is initialized with a uniform discrete distribution  $\mathcal{P}_0(\Phi_i)$  which reflects our prior ignorance of the flux to be measured. In the first step  $k = 0$ , the algorithm repeats the Bayesian learning subroutine at a zero time delay  $\tau^{(0)} = 0$  between  $\pi/2$  pulses until the probability distribution shrinks to a twice narrower interval  $I_1 \subset I_0$ , i.e.,  $\mathcal{N}(I_1) = \mathcal{N}(I_0)/2$ , satisfying  $\sum_{i \in I_1} \mathcal{P}_0(\Phi_i) \geq 1 - \epsilon_0$ . The flux values  $\Phi_i, i \notin I_1$  are discarded. After completing the first step, the algorithm searches for the optimal delay  $\tau_j$  for the next step. The next optimal Ramsey measurement requires a larger delay  $\tau^{(1)} > 0$  such that the passport  $P_p(\tau^{(1)}, \Phi_i)$ ,  $i \in I_1$ , has the largest range:  $\tau^{(1)} = \text{argmax}_{\tau_j} \Delta P(\tau_j)$  where  $\Delta P(\tau_j) = \max_{i \in I_1} P_p(\tau_j, \Phi_i) - \min_{i \in I_1} P_p(\tau_j, \Phi_i)$ . The algorithm thus sweeps over the passport data  $P_p(\tau_j, \Phi_i)$  to find the optimal delay  $\tau^{(1)}$  with maximal range  $\Delta P(\tau^{(1)})$ . Subsequently, a new distribution  $\mathcal{P}_1(\Phi_{i \in I_1}) = \mathcal{N}^{-1}(I_1)$  and  $\mathcal{P}_1(\Phi_{i \notin I_1}) = 0$  is initialized and the algorithm proceeds to the next step by running the Bayesian learning with the new optimal delay  $\tau_1$ . After  $K$  steps, the algorithm localizes  $\Phi$  within a  $2^K$  times narrower interval  $I_K$ ,  $\mathcal{N}(I_K) = \mathcal{N}(I_0)/2^K$ , with an error probability  $\epsilon = 1 - \prod_{k=0}^{K-1} (1 - \epsilon_k)$ .

**Quantum Fourier algorithm.** This algorithm starts from the Ramsey measurement with an optimal time delay  $\tau^{(s)} \sim T_2$ . The starting delay  $\tau^{(s)}$  is a free input parameter of the algorithm. Similarly to the Kitaev algorithm, the quantum Fourier algorithm runs the Bayesian learning subroutine until the flux probability distribution  $\mathcal{P}_0(\Phi_i)$ ,  $i \in I_0$ , squeezes to a twice narrower subset  $S_1 \subset I_0$  such that  $\sum_{i \in S_1} \mathcal{P}_0(\Phi_i) \geq 1 - \epsilon_0$ . However, in contrast to the Kitaev algorithm, the passport function  $P_p(\tau^{(s)}, \Phi_i)$  is an ambiguous function of  $\Phi_i$  at the large delay  $\tau^{(s)}$ . As a result,  $S_1$  is not a single interval but rather a set of  $n \sim \tau^{(s)}/\tau_0$  disjoint narrow intervals  $S_1 = I_1 \cup \dots \cup I_n$  of almost equal lengths, see Fig. 2. Hence, after completing the first step, the flux value is

distributed among  $n$  equiprobable alternatives  $I_i$ . The Fourier algorithm discriminates between these  $n$  alternatives in the next steps. First, it searches for the next optimal delay  $\tau_j$ , where it is possible to rule out half of the remaining alternatives in the most efficient way. At each delay  $\tau_j$  the algorithm splits the remaining intervals  $I_i$ ,  $i = 1, \dots, n$  into two approximately equal-in-size groups  $A = I_{i_1} \cup \dots \cup I_{i_{[n/2]}}$  and  $B = I_{i_{[n/2]+1}} \cup \dots \cup I_{i_n}$  which are ordered by the passport function,  $P_p(\tau_j, \Phi \in A) > P_p(\tau_j, \Phi \in B)$ . Then it finds the probability distance  $\Delta P(\tau_j) = \min_{i \in A} P_p(\tau_j, \Phi_i) - \max_{i \in B} P_p(\tau_j, \Phi_i) > 0$  separating the two sets  $A$  and  $B$ . Repeating this procedure at all available delays  $\tau_j$ , the algorithm finds the optimal delay  $\tau^{(1)}$  with maximal  $\Delta P(\tau_j)$  over the discrete set of delays  $\tau_j$ . In the next step, the algorithm discriminates between  $A$  and  $B$  by repeating the Bayesian learning subroutine approximately  $[\Delta P(\tau_1)]^{-2}$  times and sets  $S_2 = A$  or  $B$ . Continuing in this way, the algorithm returns a single interval  $I_{\text{out}}$  where the actual value of the flux  $\Phi(\Phi_i)$ ,  $i \in I_{\text{out}}$ , is located. Fig. 2 shows how the flux distribution function  $\mathcal{P}(\Phi_i)$  develops in time during the execution of the Kitaev and Fourier algorithms.

**Results.** The superiority of our quantum metrological algorithms is clearly demonstrated by the scaling behaviour of the magnetic flux resolution with the total *sensing time* of the flux measurement, see Fig. 3. We run each algorithm  $n = 25$  times at every flux value  $\Phi = \Phi_i$ ,  $i \in I_0$ , within the entire flux range, and find the corresponding arrays of estimated values  $\hat{\Phi}_j$ ,  $j = 1, \dots, n$ . The estimate  $\hat{\Phi} = \hat{\Phi}(\mathcal{P}(\Phi))$  is defined as the most likely value derived from the observed probability distribution  $\mathcal{P}(\Phi)$ . For a probability distribution  $\mathcal{P}_i(\Phi)$  measured at a known flux value  $\Phi = \Phi_i$  the corresponding estimate  $\hat{\Phi}_i$  is a random quantity due to statistical nature of the measurement procedure. We define an *aggregated resolution*  $\delta\Phi$  as an ensemble standard deviation of the random variables  $\hat{\Phi}_i - \Phi_i$ ,

$$\delta\Phi^2 = \frac{1}{\mathcal{N}(I_0)} \sum_{i \in I_0} \frac{1}{n-1} \sum_{j=1}^n [\hat{\Phi}_j - \Phi_i]^2. \quad (5)$$

In case of the Fourier algorithm, such a definition is meaningful only at the final step of the algorithm where  $\mathcal{P}(\Phi)$  becomes a single-peaked function. The sensing time  $t$  is defined through the total number of calls of the Bayesian learning subroutine  $m$ ,  $t = NT_{\text{rep}} m$ . The scaling behaviour of the measured flux resolution  $\delta\Phi(t)$  with sensing time  $t$  is shown in Fig. 3 for both our algorithms and is compared with the scaling  $\delta\Phi_{\text{std}}(t)$  of the standard (classical) procedure, where all Ramsey measurements are done at a zero delay  $\tau = 0$ .

Both quantum algorithms clearly outperform the standard procedure, with the Kitaev algorithm appearing slightly more efficient than the Fourier one. We explain this by the fact that the Fourier algorithm strongly relies on the periodicity of the Ramsey interference pattern given by Eq. (1), whereas our readout scheme produces a slightly distorted pattern. On the other

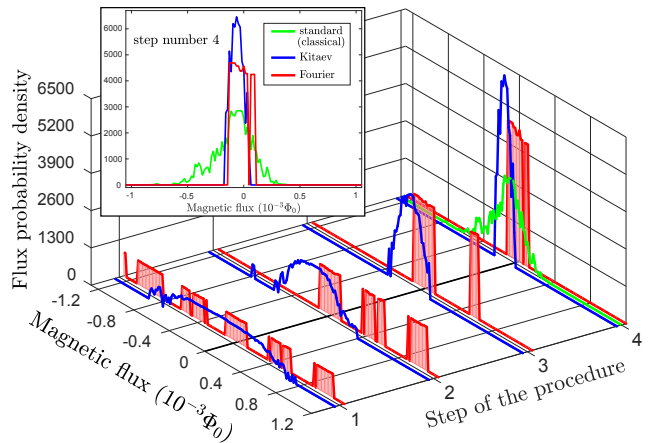


FIG. 2: Evolution of the flux probability distribution  $\mathcal{P}_k(\Phi_i - \Phi)$ , during the run of the first  $k = 1, \dots, 4$  steps of the Fourier (red panels) and Kitaev (blue curves) estimation algorithms. The magnetic flux is measured with respect to a reference flux (as explained in the Methods). The actual flux value is shown by a thick black line in the flux-step plane. The Kitaev algorithm starts at a zero delay  $\tau = 0$  and a first step returns a broad probability distribution with a single peak centered near the actual flux value. During the run of the Kitaev algorithm this peak narrows down. The Fourier algorithm starts from the Ramsey measurement at large delay  $\tau^{(s)} = 360$  ns, with the first step returning a probability distribution with six out of twelve flux intervals assuming a non-vanishing value. Hence, this first step selects half of the  $n = \tau^{(s)}/\tau_0 \sim 12$  different flux intervals  $\Delta\Phi_m$  given by  $\Delta\omega_m = \Delta\omega_0 + 2\pi i/\tau_s$ ,  $m = 0, \dots, n-1$ , where  $\Delta\omega_m \equiv \omega_{01}(\Delta\Phi_m) - \omega_d$  is the frequency interval corresponding to the flux interval  $\Delta\Phi_m$ , and determines the parity of the yet unknown index  $m \in [0, n-1]$  associated with the true flux interval. In the second step, the Fourier algorithm proceeds to a shorter delay and rules out another half of the remaining six intervals. In the next two steps the algorithm discriminates between the remaining three alternatives and ends up with the correct flux interval. The green line at the fourth step displays the probability distribution learned by the standard (classical) procedure during the same number of Ramsey measurements as was required by the quantum procedures. The distributions obtained at the step number 4 for the Kitaev and Fourier estimation algorithms and in the standard (classical) measurement are shown in the inset.

hand, the Kitaev algorithm turns out to be more stable to the irregularities in the measured passport function  $P_p(\tau, \Phi)$ . The magnetic flux sensitivities  $A_{\text{quant}}$  range within  $5.6 - 7.1 \times 10^{-6} \Phi_0 \text{ Hz}^{-1/2}$  for the Kitaev algorithm and within  $6.5 - 8.5 \times 10^{-6} \Phi_0 \text{ Hz}^{-1/2}$  for the Fourier procedure. These sensitivities are an order of magnitude worse than the theoretical bound  $4.0 \times 10^{-7} \Phi_0 \text{ Hz}^{-1/2}$  set by Eq. (3). The discrepancy has two main reasons. First, our readout scheme is not a single-shot measurement, which leads to a factor 32 increase of the  $T_{\text{rep}}$  time. Second, we spend part of the time resource for the intermediate steps with  $\tau_k \leq T_2$  during the run of the phase estimation procedure. Finally, for our trans-

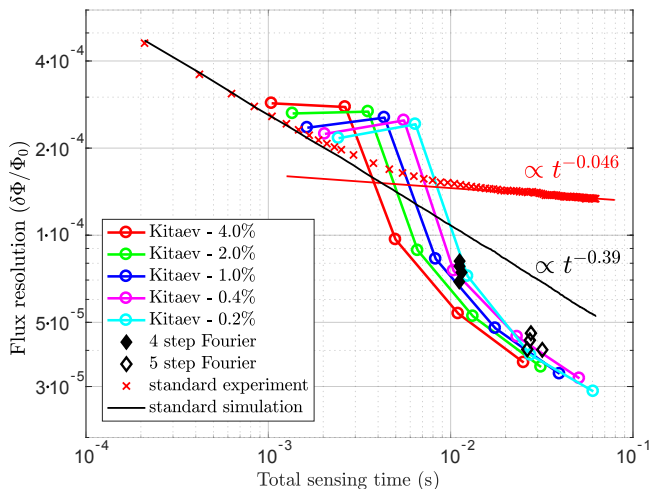


FIG. 3: Observed scaling behavior of the flux resolution versus total sensing time for the three different metrological procedures, Kitaev (colored circles), Fourier (black diamonds) and standard (red crosses). The Kitaev algorithm has been run with constant tolerances  $\epsilon_k = \epsilon$  for each step  $k = 1, \dots, 5$  and for five different values of  $\epsilon$  as indicated by different colors. The Fourier algorithm has been performed with the step-dependent tolerances  $\epsilon_k = 0.182, 0.076, 0.039, 0.02, 0.01$  for  $k = 1, \dots, 5$ . We show the result of the Fourier algorithm only for the final two steps,  $k = 4$  (filled diamonds) and  $k = 5$  (empty diamonds), running the algorithm with four different starting delays,  $\tau^{(s)} = 300, 320, 340$  and  $360$  ns (all collapsed to the same data points). The phase estimation algorithms lag behind in precision at short times when compared to the standard procedure, but rapidly gain precision at longer times. The black solid line represents the scaling law for a numerical simulation of the standard procedure with a regular passport function given by Eq. (1). The crossover to the red solid line is due to the irregularity of the passport function.

mon, the SQUID area  $S \simeq 600 \mu\text{m}^2$  results in a sensitivity in the range  $19.3 - 29.3 \text{ pT Hz}^{-1/2}$ . In practice, a transmon device with a larger SQUID area experiences a stronger dephasing due to external magnetic-field fluctuations that limit its sensitivity. For our sample with an external noise density  $S_B \simeq 0.2 \text{ pT Hz}^{-1/2}$ , the optimal SQUID size is  $S \simeq 500 \mu\text{m}^2$  at the chosen working point, see Methods.

Interestingly, the non-ideality of the qubit's passport strongly affects the performance of the standard procedure as well. Its scaling behaviour  $\delta\Phi_{\text{std}} \propto t^{-\alpha}$  exhibits a crossover in the scaling exponent  $\alpha$ , assuming a value  $\alpha \approx 0.39$  at short sensing times, while at large times  $\alpha$  decreases to a much smaller value  $\approx 0.046$ . The scaling exponent  $0.39$  deviates from the shot noise exponent  $1/2$  due to the cases when the actual flux value is located near the boundaries of the flux interval  $\Phi \in [\Phi_1, \Phi_{161}]$ , where the passport function  $P_p(0, \Phi)$  has an extremum and the scaling exponent for the standard procedure is reduced to  $1/4$ ,  $\delta\Phi(t) \propto t^{-1/4}$ . As a result, the aggregated scaling exponent of Eq. (5) is reduced below  $1/2$ .

On the other hand, the crossover to  $\alpha \approx 0.046$  is a consequence of the irregularity of the passport function set by low-frequency noise fluctuations during the passport measurement. Indeed, at large sensing times, the standard procedure needs to distinguish fluxes within a narrow interval where the passport function  $P_p(\tau = 0, \Phi)$  has a non-regular and non-monotonic dependence on  $\Phi$ . As a result, the Bayesian learning procedure fails to converge to a correct flux value. In contrast, at a larger scale of  $\Phi$ , the passport function is smooth and monotonic and the standard procedure behaves properly. These arguments are indeed confirmed by a numerical simulation with a regular passport function given by Eq. (1). Importantly, both our quantum metrological algorithms are more stable than the standard procedure with respect to passport imperfections and their scaling behaviour at large sensing times coincides with the scaling behaviour resulting from a regular passport function. The quantum algorithms suffer, however, from the same irregularity problem at larger sensing times, not shown in Fig. 3

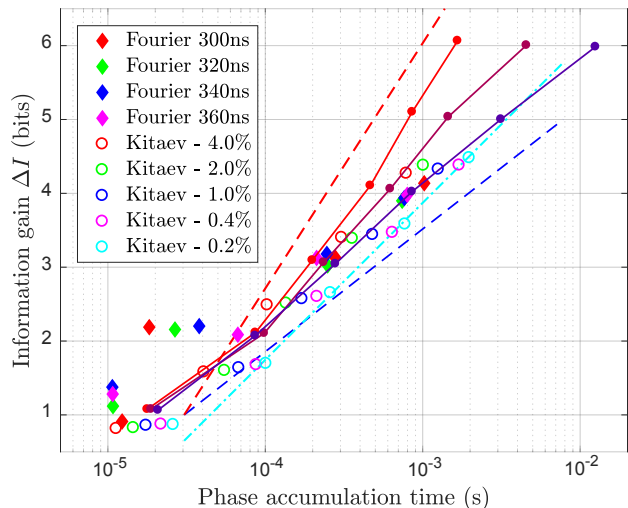


FIG. 4: Information (in bits) inferred by the Kitaev (circles) and Fourier (filled diamonds) algorithms as a function of the total phase accumulation time. The Kitaev algorithm was run for five different tolerance level constants  $\epsilon$  at each step (indicated by color). The color of diamonds indicates the different starting time of the Fourier algorithm. The dashed red and blue lines refer to the Heisenberg and shot-noise scaling laws with the corresponding scaling exponents  $1$  and  $1/2$ . The thin solid lines show the numerical simulation for the 6-step Kitaev algorithm with an idealized passport function given by Eq. (1) at different dephasing times  $T_2$  ranging from  $10 \mu\text{s}$  (red line) to  $340 \text{ ns}$  (blue line). One can clearly see that at large dephasing times the Kitaev procedure approaches the Heisenberg limit, while at smaller  $T_2$  the scaling exponent decreases to the standard quantum limit  $0.5$ . The observed experimental scaling behaviour shows that both Fourier and Kitaev algorithms are indeed quantum with a scaling exponent above the standard quantum limit  $1/2$ , see the dash-dotted cyan line connecting the Kitaev (at  $0.2\%$  tolerance) data.

Finally, we discuss how our metrological algorithms use the quantum resource of qubit coherence in order to acquire information about the measured flux. We quantify the quantum coherence resource spent in a given measurement by the total *phase accumulation time*  $\tau_\phi = N \sum_k \tau_k m_k$ , where  $m_k$  is the number of calls for the Bayesian learning subroutine with delay  $\tau_k$ . The amount of information  $\Delta I$  acquired during the measurement is given by a decrease of the Shannon entropy  $\Delta I = H(\mathcal{P}_0) - H(\mathcal{P})$ , where  $\mathcal{P}_0(\Phi_i)$  and  $\mathcal{P}(\Phi_i)$  are the initial and final probability distributions and  $H(\mathcal{P}) = -\sum_i \mathcal{P}(\Phi_i) \log_2(\mathcal{P}(\Phi_i))$ . The scaling behaviour  $\Delta I(\tau_\phi) \propto \tau_\phi^\alpha$  separates the classical domain with  $0 < \alpha \leq 0.5$  from the quantum domain with  $0.5 < \alpha \leq 1$ , where  $\alpha = 1$  corresponds to the ultimate Heisenberg limit. Indeed, in the ideal case where no relaxation and decoherence phenomena are present, the quantum algorithms improve by a factor of two the flux resolution (squeeze the flux distribution function into a twice narrower range) for each next step of the procedure. This means that the associated Shannon entropy decreases by  $\ln(2)$  and one learns one bit of information for each doubling of the Ramsey delay time. In contrast, the classical procedure after  $N \gg 1$  repetitions results in a Gaussian probability distribution of the measured quantity where the precision scales as  $\delta\Phi \propto 1/\sqrt{N}$ . Hence the associated Shannon entropy scales as  $\tau^{0.5}$  with an invested total phase accumulation time  $\tau = N\tau_0$ . We run each quantum algorithm 25 times for every flux value and average over the obtained information gains and phase times. The resulting scaling dependence is shown in Fig. 4 and demonstrates that both Kitaev and Fourier algorithms indeed belong to the quantum domain with a scaling exponent within  $[0.624, 0.654]$  (95% confidence interval). The scaling exponent is still below the Heisenberg limit, which is a consequence of the finite dephasing time  $T_2$ : at large time delays  $\tau \sim T_2$  the visibility of the Ramsey interference pattern decreases, requiring more Ramsey measurements in order to learn the next bit of information.

**Conclusions.** We have used a single transmon qubit as a magnetic-flux sensor and have implemented two quantum metrological algorithms in order to push the measurement sensitivity beyond the standard shot-noise limit. In our experiments, we re-prepare and measure the qubit's state several times, utilizing the coherent dynamics of the qubit as a quantum resource. We demonstrate experimentally, on the same sensor sample, that suitably modified Kitaev- and Fourier algorithms both outperform the classical shot-noise-limited measurement procedure and approach the Heisenberg limit. Both algorithms demonstrate a similar asymptotic flux-sensitivity  $A_\Phi \sim 6 \times 10^{-6} \Phi_0 \text{ Hz}^{-1/2}$  or magnetic-field sensitiv-

ity  $A_B \sim 20.7 \text{ pT Hz}^{-1/2}$  within a *dynamical range*  $\Delta\Phi/A_\Phi \sim 430\sqrt{\text{Hz}}$  at a coherence time  $T_2 \sim 260 \text{ ns}$  of the qubit. Finally, we can compare the characteristics of our qubit sensor with other types of existing magnetometers. DC SQUID sensors typically have  $1 \mu\Phi_0 \text{ Hz}^{-1/2}$  sensitivity and a much larger dynamical range  $\sim 10^6\sqrt{\text{Hz}}$ , see Ref. 26. However, a conventional DC SQUID is operated with a current bias just above its critical current, which limits its sensitivity to  $10^{-7} - 10^{-8} \Phi_0 \text{ Hz}^{-1/2}$  due to intrinsic thermal noise fluctuations of excited quasiparticles. Atomic magnetometers<sup>27</sup> can approach a magnetic field sensitivity  $\sim 0.1 - 1.0 \text{ fT Hz}^{-1/2}$ . However, these magnetometers measure the field in a finite macroscopic volume  $\sim 1 \text{ cm}^3$  and their sensitivity translated into a  $(100 \mu\text{m})^3$  volume range of a transmon sensor reduces to  $0.1 - 1.0 \text{ pT Hz}^{-1/2}$ , with a dynamical range  $\sim 10^4 - 10^5\sqrt{\text{Hz}}$  compatible with DC SQUID sensors. NV centers in diamond are able to resolve magnetic fields with an atomic spatial resolution and approach sensitivities  $\sim 6.1 \text{ nT Hz}^{-1/2}$ . Phase estimation algorithms allow one to enlarge the dynamical range of NV-sensors<sup>15</sup> up to  $3 \times 10^5 \text{ Hz}^{1/2}$ . The superconducting qubit sensors have a high potential for improving their characteristics. Such sensors are not prone to intrinsic noise fluctuations due to thermal quasi-particles and their sensitivity is limited only by their coherence time and duration of the readout procedure. Improving the qubit coherence time and readout efficiency, one can potentially access a few orders of magnitude higher sensitivities and dynamical ranges.

**Acknowledgements.** The work was supported by the RFBR Grant No. 17-02-00396A (G. L.), by the Pauli Center for Theoretical Studies at ETH Zurich (G. L.) and by the Swiss National Foundation through the NCCR QSIT (A. L.) and the Ministry of Education and Science of the Russian Federation 16.7162.2017/8.9 (A. L.). We acknowledge financial support from Väisälä Foundation, the Academy of Finland (project 263457 and Center of Excellence “Low Temperature Quantum Phenomena and Devices” - project 250280), and the Centre for Quantum Engineering at Aalto University. The experiments used the cryogenic facilities of the Low Temperature Laboratory at Aalto University.

**Author contribution.** The sample used in the experiment was designed and fabricated by SD. The measurements were performed by SD, AV, and AVL; the data was processed by AV and SD and further analyzed by AVL. GBL, GB, and AVL worked on the theoretical foundation of the experiments. AVL and SD wrote the first draft, with further contributions from GBL, GB, and GSP. AVL and GSP supervised the project.

<sup>1</sup> Cleve R., Ekert A., Macchiavello C. and Mosca M., ‘Quantum algorithms revisited’, Proc. Roy. Soc. A, **454**, 339

(1998).

<sup>2</sup> Shor P. W., ‘Algorithms for quantum computation: dis-

- crete logarithms and factoring’, in *Proceedings of the 35th Annual Symposium on Foundations of Computer Science* (IEEE Computer Society Press, 1994), pp 124-134.
- <sup>3</sup> Smolin J. A., Smith G. and Vargo A., ‘Oversimplifying quantum factoring’, *Nature* **499**, 163 (2013).
  - <sup>4</sup> Harrow A. W., Hassidim A., and Lloyd S., ‘Quantum algorithm for solving linear systems of equations’, *Phys. Rev. Lett.* **15**, 150502 (2009).
  - <sup>5</sup> Giovannetti V., Lloyd S. and Maccone L., ‘Quantum-Enhanced Measurements: Beating the Standard Quantum Limit’, *Science* **306**, 1330 (2004).
  - <sup>6</sup> Sekatski P., Skotiniotis M., Kolodynski J., and Dür W., ‘Quantum metrology with full and fast quantum control’, *Quantum* **1**, 27 (2017).
  - <sup>7</sup> Nagata T., Okamoto R., OBrien J. L., Sasaki K. and Takeuchi S., ‘Beating the standard quantum limit with four-entangled photons’, *Science* **316**, 726 (2007).
  - <sup>8</sup> Dowling, J. P., ‘Quantum optical metrology—the lowdown on high-N00N states’, *Contemp. Phys.* **49**, 125 (2008).
  - <sup>9</sup> Matthews J. CF, Zhou X.-Q., Cable H., Shadbolt P. J., Saunders D. J., Durkin G. A., Pryde G. J. and LOBrien J., ‘Towards practical quantum metrology with photon counting’, *NPJ Quantum Inf.* **2**, 16023 (2016).
  - <sup>10</sup> Kitaev A. Yu., ‘Quantum measurements and the Abelian stabilizer problem’, arXiv preprint quant-ph/9511026 (1995).
  - <sup>11</sup> Nielsen M. A., and Chuang I. L., ‘Quantum Computation and Quantum Information’, (*Cambridge Series on Information and the Natural Sciences*, Cambridge Univ. Press, ed. 1, 2004).
  - <sup>12</sup> van Dam W., DAriano G. M., Ekert A., Macchiavello C., and Mosca M., ‘Optimal Quantum Circuits for General Phase Estimation’, *Phys. Rev. Lett.* **98**, 090501 (2007).
  - <sup>13</sup> Waldherr G., Beck j., Neumann P., Said R. S., Nitsche M., Markham M. L., Twitchen D. J., Twamley J., Jelezko F., and Wrachtrup J., ‘High-dynamic-range magnetometry with a single nuclear spin in diamond’, *Nature Nanotechnology* **7**, 105-108 (2012).
  - <sup>14</sup> Puentes G., Waldherr G., Neumann P., Balasubramanian G. and Wrachtrup J., ‘Efficient route to high-bandwidth nanoscale magnetometry using single spins in diamond’, *Scientific Reports* **4**, 4677 (2014).
  - <sup>15</sup> Bonato C., Blok M. S., Dinani H. T., Berry D. W., Markham M. L., Twitchen D. J. and Hanson R., ‘Optimized quantum sensing with a single electron spin using real-time adaptive measurements’, *Nature Nanotechnology* **11**, 247 (2016).
  - <sup>16</sup> Monz T., Nigg D., Martinez E. A., Brandl M. F., Schindler Ph., Rines R., Wang S. X., Chuang I. L. and Blatt R., ‘Realization of a scalable Shor algorithm’, *Science* **351**, 1068 (2016).
  - <sup>17</sup> Higgins B. L., Berry D. W., Bartlett S. D., Wiseman H. M. and Pryde G. J., ‘Entanglement-free Heisenberg-limited phase estimation’, *Nature* **450**, 393 (2007).
  - <sup>18</sup> Koch J., Terri M. Yu, Gambetta J., Houck A. A., Schuster D. I., Majer J., Blais A., Devoret M. H., Girvin S. M. and Schoelkopf R. J., ‘Charge insensitive qubit design derived from the Cooper pair box’, *Phys. Rev. A* **76**, 042319 (2007).
  - <sup>19</sup> Bal M., Deng C., Orgiazzi J.-L., Ong F. R. and Lupascu A., ‘Ultrasensitive magnetic field detection using a single artificial atom’, *Nature Comm.* **3**, 1324 (2012).
  - <sup>20</sup> Yoshihara F., Harrabi K., Niskanen A. O., Nakamura Y., and Tsai J. S., ‘Decoherence of flux qubits due to  $1/f$  flux noise’, *Phys. Rev. Lett.* **97**, 167001 (2006).
  - <sup>21</sup> Cottet A., ‘Implementation of a quantum bit in a superconducting circuit’, Ph.D. thesis, Université Paris VI, (2002).
  - <sup>22</sup> Clarke J., Wilhelm F. K., ‘Superconducting quantum bits’, *Nature* **453**, 1031 (2008).
  - <sup>23</sup> Suslov M. V., Lesovik G. B., and Blatter G., ‘Quantum abacus for counting and factorizing numbers’, *Phys. Rev. A* **83**, 052317 (2011).
  - <sup>24</sup> R. B. Griffiths R. B., and Niu C.-S., ‘Semiclassical Fourier Transform for Quantum Computation’, *Phys. Rev. Lett.* **76**, 3228 (1996).
  - <sup>25</sup> Lebedev A. V., Treutlein P., and Blatter G., ‘Sequential quantum-enhanced measurement with an atomic ensemble’, *Phys. Rev. A* **89**, 012118 (2014).
  - <sup>26</sup> The SQUID Handbook: Fundamentals and Technology of SQUIDs and SQUID Systems, Vol. I (Edt. Clarke, J., Braginski, A. I., Wiley VCH Verlag GmbH & Co. KGaA, Weinheim, 2006).
  - <sup>27</sup> Budker D., Romalis M., ‘Optical magnetometry’, *Nature Physics* **3**, 227-234 (2007).

## Methods

**The superconducting artificial atom.** The transmon<sup>18</sup> is a capacitively-shunted split Cooper-pair box, with a Hamiltonian

$$H = 4E_C n^2 - E_J(\Phi) \cos(\varphi), \quad (6)$$

where  $E_C$  is the charging energy  $E_C = e^2/2C_\Sigma$  with  $C_\Sigma$  the total capacitance (dominated by the shunting capacitor). the SQUID loop in the transmon design provides a flux-dependent effective Josephson energy  $E_J(\Phi) = E_{J\Sigma} |\cos(\pi\Phi/\Phi_0)|$  (assuming identical junctions). The state of the device is described by a wavefunction which treats the superconducting relative phase across junctions  $\varphi$  as a quantum variable similar to a standard coordinate. In contrast to standard SQUID measurements, the flux dependence is reflected in the quantized energy levels; for the first transition this reads

$$\hbar\omega_{01} = \sqrt{8E_C E_J(\Phi)} - E_C. \quad (7)$$

The readout of the qubit state is realized by a dispersive coupling of the transmon to a coplanar waveguide (CPW) resonator whose resonance frequency depends on the transmon state. This allows us to perform a non-demolition measurement of the qubit state by sending a probe pulse to the CPW right after the second  $\pi/2$ -pulse and collecting the resulting resonator response signal whose shape in time depends on the qubit state, see SI 1.

**Dephasing mechanisms.** The dephasing of the qubit can be modeled via an interaction of the qubit with an external classical noise source  $\nu(t)$ . The qubit state acquires a stochastic relative phase  $\delta\phi = \int^\tau dt \nu(t) \partial\omega_{01}/\partial\nu$ . Then the decay function  $\gamma(\tau) \equiv \langle e^{i\delta\phi} \rangle$  can be expressed via a noise spectral density function  $S_\nu(\omega) = \int \langle \nu(t)\nu(t') \rangle e^{i\omega(t-t')} dt dt'$  as<sup>21</sup>  $\gamma(\tau) =$

$\exp[-\frac{1}{2}(\partial\omega_{01}/\partial\nu)^2 \int \frac{d\omega}{2\pi} S_\nu(\omega) \sin^2(\omega\tau/2)/(\omega/2)^2]$ . A white noise source with a constant spectral density  $S_\nu$  at low frequencies gives an exponential decay function  $\gamma(\tau) = \exp(-\Gamma_{\text{exp}}\tau)$  with  $\Gamma_{\text{exp}} = \frac{1}{2}S_\nu(\partial\omega_{01}/\partial\nu)^2$ . A  $1/f$ -noise  $S_\nu(\omega) = S_{1/f}/|\omega|$  gives a Gaussian decay  $\gamma(\tau) = \exp(-(\Gamma_{1/f}\tau)^2)$  with  $\Gamma_{1/f} \sim \sqrt{S_{1/f}|\ln(\omega_c\tau)|/(2\pi)}|\partial\omega_{01}/\partial\nu|$ , where  $\omega_c \sim 1/T_{\text{rep}}$  is a low frequency cut-off given by the time duration of the Ramsey sequence,  $\tau \sim 2T_1$ .

**Quantum and classical magnetic flux sensitivities.** After  $N$  Ramsey experiments at a fixed delay  $\tau$ , the probability of the excited state  $P(\tau, \Delta\omega)$  can be estimated as  $N_1/N$ , where  $N_1$  is the number of outcomes where an excited state was detected. The accuracy  $\delta P^2 = \langle (P(\tau, \Delta\omega) - N_1/N)^2 \rangle$  of this estimate is given by a binomial statistics,  $\delta P^2 = N_1(N - N_1)/N^3 \leq 1/(4N)$ . From the equation  $P(\tau, \Delta\omega) = N_1/N$ , one can find the frequency mismatch  $\Delta\omega$ . The corresponding accuracy  $\delta[\Delta\omega]$  can be found from the relation  $\delta P = |\frac{\partial P(\tau, \Delta\omega)}{\partial \Delta\omega}| \delta[\Delta\omega]$ , hence  $\delta[\Delta\omega] = |\frac{\partial P(\tau, \Delta\omega)}{\partial \Delta\omega}|^{-1} \frac{1}{2\sqrt{N}}$ . From Eq. (1), it follows that  $\min_{\Delta\omega} \left( |\frac{\partial P(\tau, \Delta\omega)}{\partial \Delta\omega}|^{-1} \right) = 2[\tau\gamma(\tau)]^{-1}e^{\tau/2T_1}$ . Combining all factors, one arrives at the flux resolution

$$[\delta\Phi] = \left| \frac{d\omega_{01}(\Phi)}{d\Phi} \right|^{-1} \delta[\Delta\omega(\Phi)] = \left| \frac{d\omega_{01}(\Phi)}{d\Phi} \right|^{-1} \frac{e^{\tau/2T_1}}{\tau\gamma(\tau)\sqrt{N}}. \quad (8)$$

The standard (classical) measurement is done at a minimal effective delay  $\tau = \tau_0 \ll T_2$ . Assuming that each Ramsey experiment takes a time  $T_{\text{rep}}$ , the flux resolution of the standard scheme is given by Eq. (2) where  $t = NT_{\text{rep}}$ . In a quantum limited measurement, one optimizes the time delay  $\tau$ . Minimizing the time factor  $[\tau\gamma(\tau)]^{-1}e^{\tau/2T_1}$  in Eq. (8), one finds the optimal time delay  $\tau^*$  from an equation  $(2T_1)^{-1} - (\ln[\gamma(\tau)])' = \tau^{-1}$ .

The magnetic field resolution  $\delta B = \delta\Phi/S \propto (S\tau^*)^{-1}$  degrades with the growth of the SQUID area  $S$  as the transmon becomes more sensitive to an external magnetic-field noise. The pure decoherence rate grows with size as  $T_\phi^{-1} \propto S_B S^2 (d\omega_{01}/d\Phi)^2$  for white magnetic noise with a constant spectral density  $S_B$ . The decoherence rate due to  $1/f$  noise grows only linearly with  $S$  and hence is less relevant. The optimal size of the SQUID area can be found by minimizing  $(S\tau^*)^{-1} \sim (2ST_1)^{-1} + S_B S (d\omega_{01}/d\Phi)^2$  with respect to  $S$ ,  $S_{\text{opt}} \sim |d\omega_{01}/d\Phi|^{-1}/\sqrt{T_1 S_B}$ . At the working point of our sample, we have  $\sqrt{S_B} \sim 0.2\text{pT Hz}^{-1/2}$  and hence  $S_{\text{opt}} \simeq 500 \mu\text{m}^2$ .

**Voltage-to-flux conversion.** The magnetic flux threading the transmon SQUID loop is generated by a dc-current flowing through the flux-bias line located nearby the SQUID loop with the current controlled by a dc-voltage  $V \in [0.977, 1.009]$  V generated with an Agilent 33500B waveform generator (see SI 2). As a result, our device can also be operated as a sensitive voltmeter. The conversion from voltage values to the non-integer part of

the normalized flux  $(\Phi/\Phi_0 - n)$ , where  $n$  is an integer number, is obtained from spectroscopic measurements (Fig. 1a), and has the form

$$\left( \frac{\Phi(V)}{\Phi_0} - n \right) = \frac{V}{V_0} + \frac{\Phi_{\text{tr}}}{\Phi_0}. \quad (9)$$

Here,  $V_0$  is the periodicity (in volts) of the CPW resonator and qubit spectra, which corresponds to the magnetic flux change by one flux quantum, and  $\Phi_{\text{tr}}$  is the residual flux trapped in the SQUID loop. Measuring the CPW resonator spectrum periodicity (see Fig. 1a inset), one finds  $V_0 = (12.55 \pm 0.05)$  volts, and the trapped flux value can be found from the position of the qubit spectrum maximum  $\omega_{01}[\Phi(V)]$  (Fig. 1a), which gives  $\Phi_{\text{tr}}/\Phi_0 = 0.059 \pm 0.004$ . Hence, our qubit based magnetic flux sensor measures a flux change relative to some reference value.

# Supplementary Information for "Quantum-enhanced magnetometry by phase estimation algorithms with a single artificial atom"

## S1. The sample and the qubit detection scheme

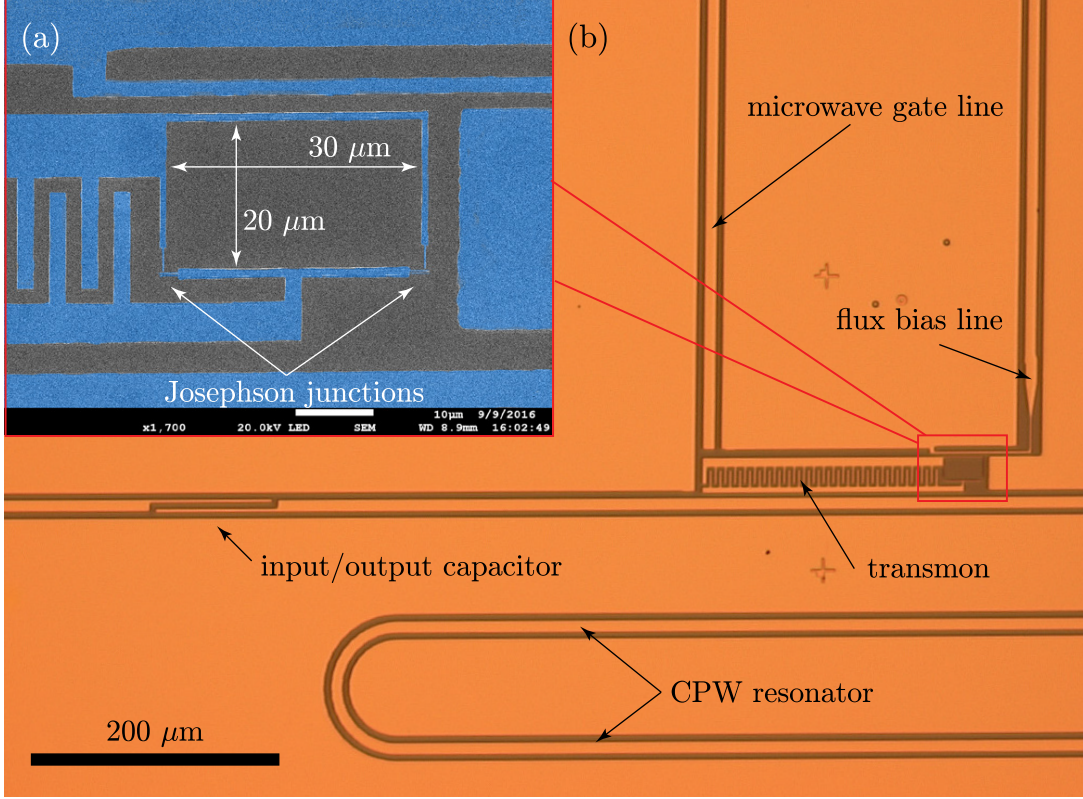


FIG. 5: (a) SEM image of the transmon SQUID loop (false colors). (b) Optical microphotograph of the sample.

The sample (see Fig. (5)) is fabricated using the standard double-angle shadow deposition technique where first 30 nm and then 60 nm of aluminum was evaporated on the pure high resistive silicon substrate at angles of  $\pm 30^\circ$  correspondingly. This is followed by the lift-off process.

The measurement of the qubit state is realized with homodyne detection by sending a  $2 \mu\text{s}$  probe pulse of a rectangular shape with a  $\nu_{\text{pr}}$  carrier frequency into the resonator immediately after the second  $\pi/2$  pulse of the Ramsey sequence. The reflected back from the resonator signal is down-converted to a slowly varying response  $r(t)$ , which is recorded by a data acquisition card with 1 ns resolution. The calibration of the readout scheme is done at a fixed flux value  $\Phi_{\text{cal}}$ , corresponding to a dc-voltage bias  $V_{\text{cal}} = 0.98 \text{ V}$  at the qubit flux bias line where the frequency mismatch  $\Delta\omega(\Phi_{\text{cal}})$  approximately vanishes. At this specific flux point we prepare the qubit in the ground  $|0\rangle$  and in the excited state  $|1\rangle$  and record the corresponding response signals  $r_{0,1}(t)$ . For each of these basis states we average over  $N_{\text{cal}} = 30 \times 65000$  separate response curves and find the averaged time traces  $\bar{r}_{0,1}(t)$ . This averaging is done in order to increase the signal-to-noise ratio. In order to optimize the readout scheme we sweep the probe pulse frequency  $\nu_{\text{pr}}$  and find the point where the area between ground and excited state response curves

$$A_{01} = \int_{t_0}^{t_1} dt |\bar{r}_0(t) - \bar{r}_1(t)| \quad (10)$$

is maximal. In our setup the optimal probe pulse frequency was  $\nu_{\text{pr}} = 5.1254 \text{ GHz}$ , and we take  $t_0 = 80 \text{ ns}$  and  $t_1 = 1800 \text{ ns}$  counted from the beginning of the probe pulse.

For a qubit prepared in an arbitrary superposition  $|\psi\rangle = \alpha|0\rangle + \beta|1\rangle$  the probe pulse projects the qubit either into the ground or excited state. The corresponding response curve  $r(t)$  is either  $\bar{r}_0(t) + \nu(t)$  or  $\bar{r}_1(t) + \nu(t)$  if the qubit was projected into the ground or excited state. Here  $\nu(t)$  is the noise in the measurement setup, which includes the added noise of the amplifiers chain (a low-noise cryogenic amplifier placed at the 4K plate of the dilution refrigerator and two microwave room temperature amplifiers). Our readout scheme returns a variable

$$h = \frac{1}{A_{01}} \int_{t_0}^{t_1} dt (r(t) - \bar{r}_0(t)) \text{sgn}(\bar{r}_1(t) - \bar{r}_0(t)) \equiv s + \xi, \quad (11)$$

where  $s$  is a discrete random variable which gets values 0 or 1 with probabilities  $|\alpha|^2$  and  $|\beta|^2$  correspondingly;  $\xi$  is a random Gaussian variable

$$\xi = \frac{1}{A_{01}} \int_{t_0}^{t_1} dt \nu(t) \text{sgn}(\bar{r}_1(t) - \bar{r}_0(t)). \quad (12)$$

We prepare and measure the qubit  $N$  times and collect  $N$  readouts  $h_i$ ,  $i = 1, \dots, N$ . Then, according to a central limit theorem at large  $N$  the averaged readout  $h_N = \frac{1}{N} \sum_{i=1}^N h_i$  is a normally distributed random variable,

$$p(h_N) = \frac{1}{\sqrt{2\pi}\sigma_N} \exp\left(-\frac{(h_N - |\beta|^2)^2}{2\sigma_N^2}\right), \quad \sigma_N^2 = \frac{\sigma_1^2 + |\alpha|^2|\beta|^2}{N}, \quad \sigma_1^2 = \langle \xi^2 \rangle. \quad (13)$$

For a large  $N \gg 1$ , the distribution function  $p(h_N)$  is peaked near the probability of the excited state  $|\beta|^2$ . The noise variance  $\sigma_1^2$  can be measured directly by reading out  $h$  for the qubit prepared either in the ground  $|\alpha|^2 = 1$  or excited  $|\beta|^2 = 1$  states. It turns out that in our setup we have  $\sigma_1^2 \approx 1.5$ .

## S2. Qubit passport measurement

We refer to the measured value of the readout variable  $h_N$  after  $N$  Ramsey sequences with a delay  $\tau$  for a given flux  $\Phi$  as a qubit's 'passport' function  $P_p(\tau, \Phi) = h_N(\tau, \Phi)$ . We use for the passport measurement  $N = 65000$  and digitise the parameter space  $(\tau, \Phi)$  into 241 time delay points  $\tau_n$ ,  $n = 0, \dots, 240$ , and 161 magnetic flux points  $\Phi_m$ ,  $m = 1, \dots, 161$ . The time delay points are separated by 2 ns time step with  $\tau_0 = 0$  ns and  $\tau_{240} = 480$  ns. The magnetic flux  $\Phi$  is controlled by a dc-voltage bias applied to the flux bias line. This voltage bias is produced by an Agilent 33500B waveform generator with high stability OCXO timebase, which has 12 mV absolute-voltage accuracy at the 1 V output level. The precision of this device is well below 0.2 mV, which is the step between the chosen 161 equidistant voltage values  $V_m$ ,  $m = 1, \dots, 161$  with  $V_1 = 0.977$  V and  $V_{161} = 1.009$  V. In our experiment we keep the drive frequency of Ramsey sequence microwave pulses constant at  $\omega_{\text{dr}} = 2\pi \times 7.246$  GHz. At every flux value  $\Phi(V_m)$  we measure a passport curve  $P_p(\tau_n, \Phi(V_m))$ .

We fit the measured passport curves  $P_p(\tau_n, \Phi(V_m))$  by two types of fit functions: one with an exponential decay,

$$P_m^{(exp)}(\tau) = \alpha_m + \beta_m \exp(-\gamma_m \tau) \cos(\omega_m \tau + \varphi_m), \quad (14)$$

and another with a Gaussian decay function combined with an exponential relaxation factor,

$$P_m^{(gauss)}(\tau) = \alpha_m + \beta_m \exp(-\tau/(2T_1) - (\tau/T_\phi)^2) \cos(\omega_m \tau + \varphi_m). \quad (15)$$

The fit results at different bias voltage points are shown in Fig. 7 at the sweet spot of the qubit spectrum and at the bias point, where our metrological experiment was done. For our sample we can not distinguish between two fit functions Eq. (14) and (15) and in the following we use an exponential decay fit function given by Eq. (14).

It turns out that among five fitting parameters  $\alpha_m$ ,  $\beta_m$ ,  $\gamma_m$ ,  $\omega_m$  and  $\varphi_m$ ,  $m = 1, \dots, 161$  the decay rate  $\gamma_m$  is almost insensitive to the flux  $\Phi(V_m)$  and we keep it constant at  $\gamma_m^{-1} = 260 \pm 30$  ns. We observe a clear linear dependence of the frequency  $\omega_m$  and phase  $\varphi_m$  on the voltage bias, see Fig. 8 and 9. The corresponding linear fits are,

$$\omega_m = 2\pi \times (423V_m - 411)\text{MHz}, \quad \varphi_m = 78.6V_m - 76.5. \quad (16)$$

The observed linear dependence of  $\omega_m$  is natural: we operate the qubit in a linear regime where its transition frequency  $\omega_{01}(\Phi)$  depends linearly on the magnetic flux and hence on the applied voltage  $V$ . From the spectroscopy measurements of the transition frequency  $\omega_{01}$  one can estimate the sensitivity  $\frac{d\omega_{01}}{dV} \approx -2\pi \times 422$  MHzV<sup>-1</sup> at  $V = 0.98$

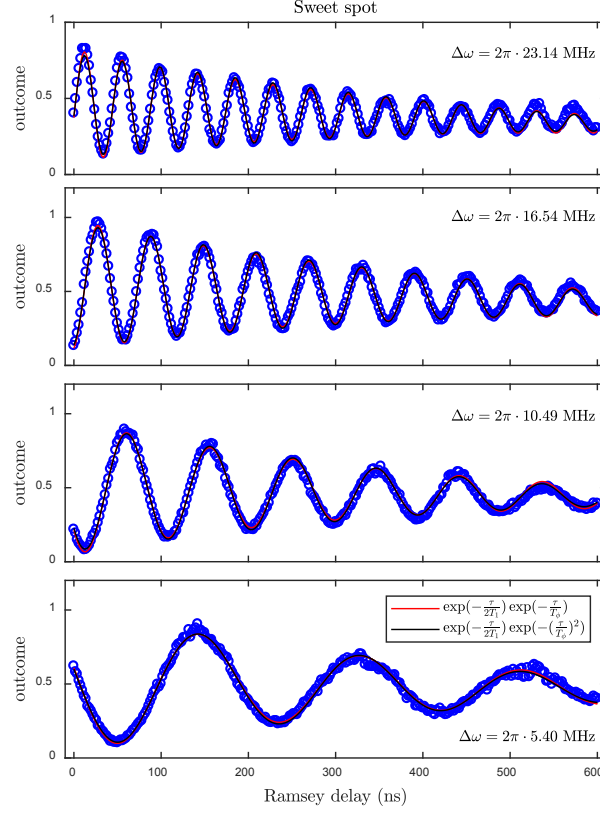


FIG. 6: **a)** Measurement of a free-induction decay near the sweet spot of the qubit spectrum at four different flux values corresponding to the frequency detunings:  $\Delta\omega = \omega_{\text{dr}} - \omega_{01}(\Phi)$ . The observed experimental curves are fitted by the exponential decay function with (red) and the Gaussian decay function (black). The pure dephasing times for an exponential decay model are  $T_\phi = 1431, 1042, 1374$  and  $887\text{ns}$  (from top to bottom) while for the Gaussian decay model we have  $T_\phi = 853, 696, 850$  and  $678\text{ns}$ .

$V$ , which is in a good agreement with a linear fit (16). The phase  $\varphi_m$  is mostly accumulated during the application of two  $\pi/2$  microwave pulses of the Ramsey sequence,

$$\varphi_m = \omega_m \tau_0 + \delta\varphi, \quad (17)$$

where  $\tau_0$  is a time parameter which defines an effective duration of two  $\pi/2$  microwave pulses,  $\delta\varphi$  is a residual flux independent phase. Then  $\tau_0 = \frac{d\varphi_m}{d\omega_m} \approx 31.6$  ns. The residual phase  $\delta\varphi$  is normally distributed with a mean value  $-0.095$  and a standard deviation  $0.055$ .

The fitting parameters  $\alpha(V_m)$  and  $\beta(V_m)$  have a weak linear dependence, see Fig. 10 and ??,  $\alpha_m = 2.75V_m - 2.21$  and  $\beta_m = 3.11V_m - 2.56$ . Both  $\alpha$  and  $\beta$  have the same tendency: these parameters increase as the voltage grows. We argue that the origin of this dependence is the CPW resonator-qubit coupling. Indeed, the bare eigenfrequency of the resonator  $\omega_{\text{res}}$  is renormalized by the qubit coupling:  $\omega_{\text{res}} \rightarrow \omega_{\text{res}} - \chi_{12}/2$ , where  $\chi_{12}$  is a resonator's partial dispersive shift,

$$\chi_{12} = \frac{2g_{01}^2}{\omega_{01}(\Phi) - \omega_C - \omega_{\text{res}}}, \quad (18)$$

where  $g_{01} \sim 2\pi \times 100$  MHz is the resonator-qubit coupling constant found from the spectroscopy measurement,  $\omega_C = 2\pi \times 299$  MHz is a frequency associated with the charging energy of the transmon:  $\omega_C = E_C/\hbar$ . In the measured flux interval  $[\Phi(V_1), \Phi(V_{161})]$  the qubit transition frequency  $\omega_{01}(\Phi)$  varies within a  $\Delta\omega_{01} \approx -2\pi \times 13.5\text{MHz}$  interval. Then according to Eq. (18) the resonator's frequency changes within

$$\Delta\omega_{\text{res}}(\Phi) = \frac{1}{2} \frac{\partial\chi_{12}}{\partial\omega_{01}} \Delta\omega_{01} = -\frac{g_{01}^2}{(\omega_{01}(\Phi) - \omega_C - \omega_{\text{res}})^2} \Delta\omega_{01} \approx 2\pi \times 41 \text{ kHz} \quad (19)$$

that is compatible with the resonance width  $\sim 550$  kHz. In the passport measurement the calibration of the readout scheme is done at a fixed flux value corresponding to  $V_{\text{cal}} = 0.98$  V. During the passport measurement the flux changes

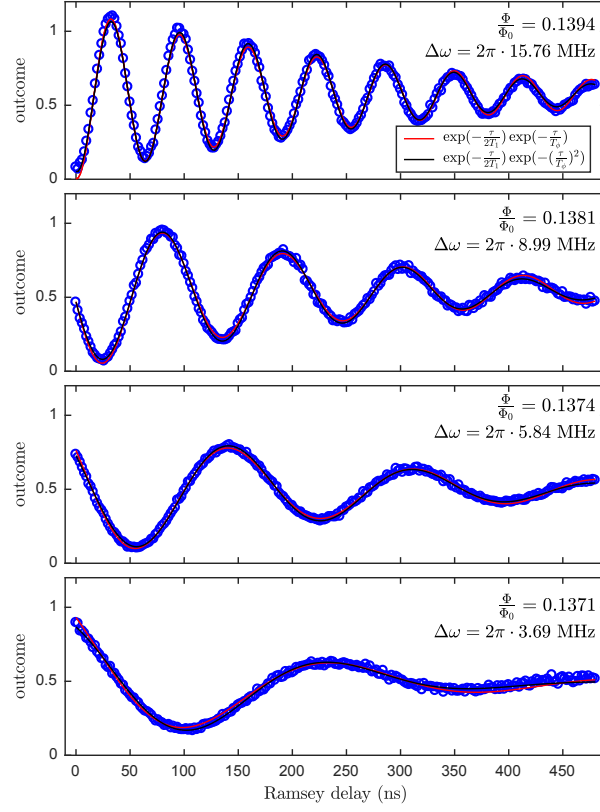


FIG. 7: **b)** Measurement of a free-induction decay near the bias point at four different magnetic flux values from the range used for the "passport" measurement shown in the Fig. (1b) of the article main text. The red lines are the fits with the exponential decay  $T_\phi = 567, 491, 450$  and  $259$ ns (from top to bottom), the black lines are the Gaussian fits  $T_\phi = 453, 424, 417$  and  $282$ ns.

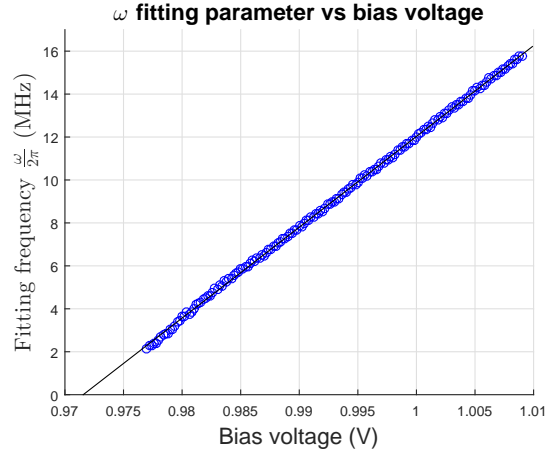


FIG. 8:

from the calibration point and hence changes the resonator's frequency as well. As a result, at a given flux value  $\Phi(V)$  the true calibration response traces  $\bar{r}_0(t|V)$  and  $\bar{r}_1(t|V)$  are different from the response traces  $\bar{r}_0(t|V_{\text{cal}})$  and  $\bar{r}_1(t|V_{\text{cal}})$  used in the readout scheme, see Supplementary Information 1. Therefore, the readout variable, see Eq. (11), might systematically deviate from the true probability of the excited state for the fluxes far away from the calibration point.

These arguments are confirmed by a direct measurement of the resonator's responses at the probe frequency  $\nu_{\text{pr}} = 5.12540$  GHz used in the experiment and at a frequency shifted by 50 kHz, namely at 5.12545 GHz. The response traces are indeed different, see Fig. 12, and therefore the readout variable  $h_N$  for the qubit prepared in the

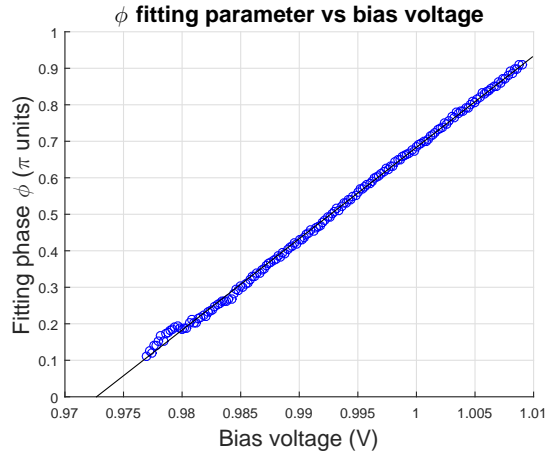


FIG. 9:

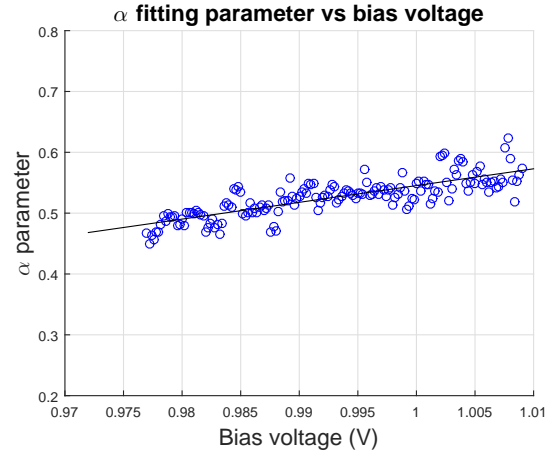


FIG. 10:

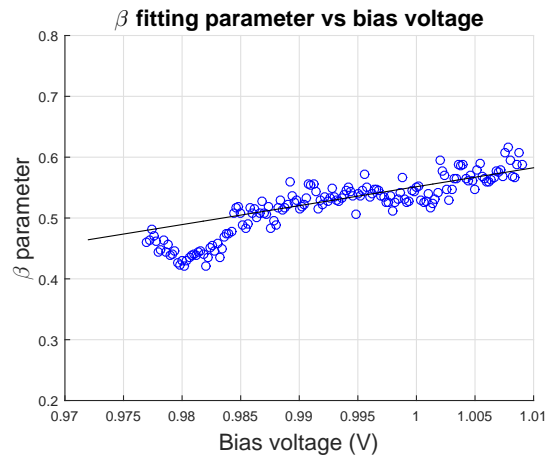


FIG. 11: The dependencies of the Eq. (14) fitting parameters (blue curves) on the flux bias voltage and their linear fits (solid lines).

excited state gets a value higher than 1,

$$h_N = \frac{\int_{t_0}^{t_1} dt (\bar{r}_1(t|V) - \bar{r}_0(t|V_{\text{cal}})) \text{sgn}(\bar{r}_1(t|V_{\text{cal}}) - \bar{r}_0(t|V_{\text{cal}}))}{\int_{t_0}^{t_1} dt |\bar{r}_1(t|V_{\text{cal}}) - \bar{r}_0(t|V_{\text{cal}})|} \approx 1.15 > 1. \quad (20)$$

Hence, at a given flux the readout variable  $h_N$  is not a true probability of the excited state, but rather a quantity which is proportional to it.

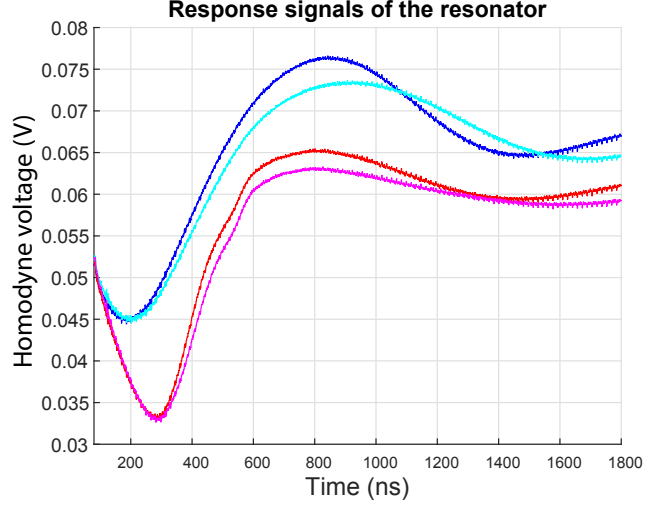


FIG. 12: Homodyne response traces measured at a probe frequency 5.12540 GHz (for the ground state (blue curve) and the excited state (red curve)), and their counterparts measured at the shifted probe frequency of 5.12545 GHz (for the ground state (cyan curve) and the excited state (magenta curve)).

### S3. Modified Kitaev phase estimation algorithm

Here we describe in detail our modified versions of the Kitaev and the Fourier phase estimation algorithms. Both algorithms exploit the pre-measured qubit's discrete passport function  $P_p(\tau_n, \Phi_m)$ . The elementary subroutine used in both algorithms is the Bayesian update procedure,

```

function BayesianUpdate( $\mathcal{P}, \tau$ )
   $h_N \leftarrow \text{GetOutcome}(\tau, N)$ ;
   $\forall m : \mathcal{P}(\Phi_m) \leftarrow \mathcal{P}(\Phi_m) \exp\left(-\frac{(h_N - P_p(\tau, \Phi_m))^2}{2\sigma_N^2}\right)$ ;
   $\forall m : \mathcal{P}(\Phi_m) \leftarrow \mathcal{P}(\Phi_m) / \sum_n \mathcal{P}(\Phi_n)$ ;
  return  $\mathcal{P}(\Phi_m)$ ;
end function

```

It takes as an input two parameters: i) the current flux probability distribution  $\mathcal{P}(\Phi_m)$  and ii) Ramsey delay time parameter  $\tau$ .  $N$  sequences of Ramsey pulses with the delay  $\tau$  is generated and the value of the readout variable  $h_N$  is measured. Then the Bayesian procedure uses the obtained measurement outcome together with the passport function and updates the flux probability distribution according to the Bayes rule. Finally, the updated distribution is normalized.

Our Kitaev phase estimation algorithm has two input parameters: number of successive steps  $K$  and a tolerance  $\epsilon > 0$ , which defines the accuracy of the procedure at each its step. The algorithm has the form

```

function KitaevProcedure( $K, \epsilon$ )
   $S = [1, \dots, 161]$ ;
   $\tau = 0$ ;

```

```

for  $k = 1, \dots, K$  do
   $\forall m \in S : \mathcal{P}(\Phi_m) = 1/\mathcal{N}(S);$ 
   $\forall m \notin S : \mathcal{P}(\Phi_m) = 0;$ 
  repeat
     $\mathcal{P} \leftarrow \text{BayesianUpdate}(\tau, N);$ 
     $S = S_{0.5}^> \cup S_{0.5}^<;$ 
  until  $\sum_{m \in S_{0.5}^<} \mathcal{P}(\Phi_m) > \epsilon$ 
   $S \leftarrow S_{0.5}^>;$ 
   $\tau \leftarrow \text{NextOptimalDelayKitaev}(S);$ 
end for
return  $\text{argmax} \mathcal{P}(\Phi_m);$ 
end function

```

In the beginning, the algorithm initializes a uniform discrete flux probability distribution  $\mathcal{P}(\Phi_m)$  for a given initial set of indexes  $m \in S = [1, \dots, 161]$  which enumerate flux values  $\Phi_m$  used for the passport measurement. At the first step ( $k = 1$ ) the algorithm repeats the Bayesian update procedure with a minimal delay  $\tau = 0$  until the probability distribution  $\mathcal{P}(\Phi_m)$  squeezes into an index subset  $m \in S_{0.5}^> \subset S$  which is twice smaller than the original set  $S$ :  $\mathcal{N}(S_{0.5}^>) = \lceil \mathcal{N}(S)/2 \rceil$  ( $\lceil x \rceil \geq x$  denotes the nearest integer bigger than the number  $x$ )

$$S = S_{0.5}^> \cup S_{0.5}^<, \quad \mathcal{P}(\Phi_m) > \mathcal{P}(\Phi_n) \quad \forall m \in S_{0.5}^>, \quad \forall n \in S_{0.5}^<, \quad (21)$$

where  $\mathcal{N}(S)$  denotes the number of elements in the set  $S$ . The update procedure repeats until the sum of the probabilities  $\sum_{m \in S_{0.5}^<} \mathcal{P}(\Phi_m)$  gets smaller than  $\epsilon$ . Then the algorithm assumes that the measured flux is located within a set  $\Phi_m$ ,  $m \in S_{0.5}^>$  with probability  $1 - \epsilon$  and resets the flux probability distribution to be uniform on the remaining set of indexes. In our version of the Kitaev algorithm, the time delay  $\tau$  of the Ramsey sequence serves as an adaptive parameter. Its value is dynamically adjusted for the next steps  $k > 1$  of the procedure by a function

```

function NextOptimalDelayKitaev( $S$ )
  for  $\tau = 0, \dots, T_2$  do
     $\Delta P(\tau) = \max_{m \in S} P_p(\tau, \Phi_m) - \min_{m \in S} P_p(\tau, \Phi_m);$ 
  end for
  return  $\text{argmax} \Delta P(\tau);$ 
end function

```

which sweeps the passport function  $P_p(\tau, \Phi_m)$  and for every delay  $\tau$  finds a probability range  $\Delta P(\tau)$  on the set of indexes  $m \in S$ . The next optimal Ramsey delay corresponds to the delay  $\tau$  where the probability range is maximal. After  $K$  steps the measured flux value is localized with a probability  $(1 - \epsilon)^K$  within a flux interval which is  $2^K$  times shorter than the initial flux interval.

#### S4. Modified Fourier phase estimation algorithm

Our version of the Fourier phase estimation algorithm has the form

```

function FourierProcedure( $K, \{\epsilon_1, \dots, \epsilon_K\}, \tau_s$ )
   $S = [1, \dots, 161];$ 
   $\forall m \in S : \mathcal{P}(\Phi_m) = 1/\mathcal{N}(S);$ 
  repeat
     $\mathcal{P} \leftarrow \text{BayesianUpdate}(\tau_s, N);$ 
     $S = S_{0.5}^> \cup S_{0.5}^<;$ 
  until  $\sum_{m \in S_{0.5}^<} \mathcal{P}(\Phi_m) > \epsilon_1$ 

   $S \leftarrow S_{0.5}^>;$ 

  for  $k = 2, \dots, K$  do
     $\forall m \in S : \mathcal{P}(\Phi_m) = 1/\mathcal{N}(S);$ 

```

```

 $\forall m \notin S : \mathcal{P}(\Phi_m) = 0;$ 
 $(\tau, A, B) \leftarrow \text{NextOptimalDelayFourier}(S);$ 

repeat
   $\mathcal{P} \leftarrow \text{BayesianUpdate}(\tau, N);$ 
   $p_a = \sum_{m \in A} \mathcal{P}(\Phi_m);$ 
   $p_b = \sum_{m \in B} \mathcal{P}(\Phi_m);$ 
until  $\min\{p_a, p_b\} > \epsilon_k$ 

if  $p_a > p_b$  then
   $S \leftarrow A;$ 
else
   $S \leftarrow B;$ 
end if

end for
return  $\text{argmax} \mathcal{P}(\Phi_m);$ 
end function

```

Differently from the Kitaev algorithm, the Fourier algorithm starts the Bayesian update procedure at some large time delay  $\tau_s \sim T_2$ . At large time delays the passport function  $P_p(\tau, \Phi)$  is not a monotonic function of  $\Phi$ . As a result, after the first step the flux probability distribution  $\mathcal{P}(\Phi_m)$  has several narrow peaks (see the main text). Each peak corresponds to a different alternative in a measured flux value and widths of the peaks define the final measurement accuracy. At the next steps,  $k = 2, \dots, K$  the Fourier procedure discriminates between these alternatives and reveals at the end of the measurement only a single peaked flux distribution. This logic changes the way in which the Fourier algorithm searches for the next optimal delay:

```

function NextOptimalDelayFourier( $S$ )
   $N \leftarrow \mathcal{N}(S);$ 
  for  $\tau = 0, \dots, \tau_s$  do
     $p = \{P_p(\tau, \Phi_{m_1}) \geq P_p(\tau, \Phi_{m_2}) \geq \dots \geq P_p(\tau, \Phi_{m_N})\};$ 
     $A(\tau) \leftarrow \{m_i, \quad i = 1, \dots, \lfloor \frac{N}{2} \rfloor\};$ 
     $B(\tau) \leftarrow \{m_i, \quad i = \lfloor \frac{N}{2} \rfloor + 1, \dots, N\};$ 
     $\Delta p_{A,B}(\tau) \leftarrow P_p(\tau, \Phi_{\lfloor \frac{N}{2} \rfloor}) - P_p(\tau, \Phi_{\lfloor \frac{N}{2} \rfloor + 1});$ 
  end for

   $\tau = \text{argmax}_\tau \Delta p(\tau);$ 
  return  $(\tau, A(\tau), B(\tau));$ 
end function

```

The *NextOptimalDelayFourier*( $S$ ) function takes the set of remaining indexes  $S$  and sweeps over the passport function. At every time delay  $\tau$  it orders the probability values  $P(\tau, \Phi_m)$ ,  $m \in S$  and splits  $S$  into two approximately equal in size subsets:  $S = A \cup B$ , where  $P_p(\tau, \Phi_{m \in A}) > P_p(\tau, \Phi_{m \in B})$ . The optimal time delay  $\tau$  corresponds to a delay where the probability distance  $\Delta p_{A,B}(\tau) = \min_{m,n} [P_p(\tau, \Phi_{m \in A}) - P_p(\tau, \Phi_{n \in B})]$  between two subsets is maximal. Then the function *NextOptimalDelayFourier*( $S$ ) returns three values: the optimal time delay  $\tau$ , and two corresponding subsets of indexes  $A(\tau)$  and  $B(\tau)$ . Then the Fourier algorithm runs the Bayesian update procedure at the optimal delay  $\tau$  and discriminates between two alternatives for the flux to be localized either in  $A$  or in  $B$  with an error probability given by the input parameter  $\epsilon_k$ . Proceeding in this manner the Fourier algorithm in  $K - 2$  steps discriminates between the remaining alternatives and finally returns the most probable value of the flux.

---